Preprints of the 21st IFAC World Congress (Virtual)
Berlin, Germany, July 12-17, 2020

A Complete Process For Shipborne Sea-Ice Field Analysis Using Machine Vision ⋆

Andrei Sandru * **Heikki Hyyti** ** **Arto Visala** *
Pentti Kujala ***

* *Department of Electrical Engineering and Automation, Aalto University, Espoo, Finland (e-mail: firstname.lastname@aalto.fi).*
** *Finnish Geospatial Research Institute, National Land Survey of Finland (e-mail: firstname.lastname@iki.fi).*
*** *Department of Mechanical Engineering, Aalto University, Espoo, Finland (e-mail: firstname.lastname@aalto.fi)*

Abstract: A sensor instrumentation and an automated process are proposed for sea-ice field analysis using ship mounted machine vision cameras with the help of inertial and satellite positioning sensors. The proposed process enables automated acquisition of sea-ice concentration, floes size and distribution. The process contains pre-processing steps such as sensor calibration, distortion removal, orthorectification of image data, and data extraction steps such as sea-ice floe clustering, detection, and analysis. In addition, we improve the state of the art of floe clustering and detection, by using an enhanced version of the k-means algorithm and the blue colour channel for increased contrast in ice detection. Comparing to manual visual observations, the proposed method gives significantly more detailed and frequent data about the size and distribution of individual floes. Through our initial experiments in pack ice conditions, the proposed system has proved to be able to segment most of the individual floes and estimate their size and area.

Keywords: machine vision, sea ice, ship, k-means, dynamic thresholding, vignetting, IMU

1. INTRODUCTION

Sea-ice field analysis is important in multiple areas, such as environmental (e.g. track seasonal changes in ice coverage), logistics (e.g. path planning) or ship maintenance. With an increase in demand for shipborne transport, new transit routes in polar regions are being explored, which is the case for example of the Polar Silk Road described in Tillman et al. (2018). However, this presents new challenges, both for the vessels themselves and their human companion.

Currently, navigation through ice-infested waters requires a high degree of expertise and experience, and may present a serious threat. At the same time, shipborne ice observations are done by volunteers, thus subject to personal interpretations.

Ice field analysis may be performed by different means. In each case, however, because of the non-uniformity and even arbitrariness of the measured natural environment, a number of challenges arise. For instance, satellite based ice field analysis, classified under remote sensing, offer a wide area coverage, however, can only provide sparse spatial and temporal resolutions. On a local scale, such analysis may be performed using aerial or ship-based images. Paget et al. (2001), and Zhang and Skjetne (2015) use a combination of thresholding and morphological operations, as well as the K-means algorithm in the second case, for detecting ice floes from aerial images. Weissling et al. (2009) includes orthorectification through Ground Control Points, band thresholding and K-means algorithm. In all presented cases, the orthorectification process could be improved greatly, as well as the automation level.

In our work, a first approach is developed towards a complete system for performing automatic shipborne ice-field analysis, which focuses on obtaining total ice concentration and sea-ice floes dimensions in a predefined area in front of the ship's bow and in pack ice conditions (see Fig. 6a as an example). Selected ideas from previous works are used (such as thresholding and K-means), and novelty techniques introduced (such as orthorectification using rotation matrices and an inertial measurement unit (IMU), and a modified version of the K-means algorithm, namely Dynamic Thresholding or DT in short). In addition, we show that the blue channel from an RGB camera is most suited for the segmentation task and an experimental system for recording data is proposed.

In the next section, we propose the methodology needed to analyse the data coming from the experimental setup on a ship and obtain the ice floe analysis results in Section 3. Then, we discuss the results in Section 4.

⋆ Strategic Research Council at the Academy of Finland is acknowledged for financial support of project "Competence-Based Growth Through Integrated Disruptive Technologies of 3D Digitalization, Robotics, Geospatial Information and Image Processing/Computing - Point Cloud Ecosystem" (project decision numbers 293389 and 314312).

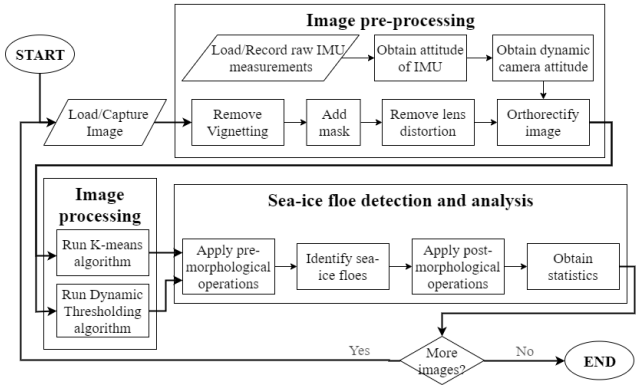

Fig. 1. Overview of the proposed complete process for sea-ice field analysis

2. METHODS

The proposed complete process for performing ice field analysis, by means of machine vision, is presented in Fig. 1. The order in which the operations are executed is crucial, since they alter the imagery data and hence directly influence the behaviour of all the subsequent operations. In the following subsections, each part of the process and their related methods are described.

2.1 Image pre-processing

Before attempting to perform an analysis to detect and measure sea-ice floes, images need to undergo a series of operations, in which camera artifacts are removed and images are geometrically rectified, such that they present an approximated *true horizontal shape* of the floes (i.e. as seen perpendicularly from above).

Remove vignetting. Vignetting effect is a systematic flaw which attenuates optical rays with larger span-off angle from the camera's principal axis (i.e. pixels tend to appear darker the further they are from the image's optical centre). Since it is systematic, it can be modelled and removed. We built on top of selected ideas from Zheng et al. (2008); Lyu (2010); Kang and Weiss (2000), a number of assumptions were made: the vignetting effect is radial around the optical centre of an image and it can be extracted from a flat, texture-less surface.

At first, the camera lens was covered with a semi-transparent, homogeneous material, then pointed at a texture-less surface in controlled lighting conditions. Next, a set of 12 images were taken and pixel-wise averaged. In this fashion, an empirical representation of the camera's vignetting effect is obtained.

The empirical mask from the previous step was divided in four quadrants and used to produce a plot of pixel intensity versus radial distance (i.e. Euclidean distance) to the known optical centre. The division in quadrants serves for visualization purposes only and the result can be seen in Fig. 2, where the radial behaviour of the vignetting effect becomes apparent.

Next, the data from Fig. 2 was fit with a smoothing spline parametric equation, and the result plot in the same figure as a pink line. Lastly, the inverse operation

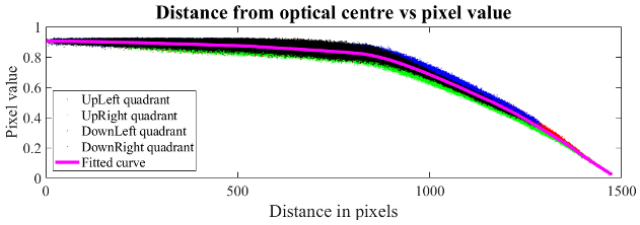

Fig. 2. Plot of pixel intensity vs. radial distance to the optical centre. Superimposed as a magenta line, a fit smoothing spline.

is followed: aforementioned fit equation is fed with the radial distances of pixels in a blank image, obtaining their intensity value. Such image is the estimated de-vignetting mask, henceforth referred to as simply DV, and depicted in 6b.

In order to remove the vignetting effect, an image is divided by DV, followed by a normalization operation using the maxima and minima pixel intensities from the original image.

Add mask. The second step involves removing all the elements which are alien to the analysis, to prevent them from influencing it (e.g. in this case, the ship). This operation can be expressed using the Hadamard pixel-wise product as:

$$O = I \circ M, \tag{1}$$

where I and O are the input and output images, respectively; and M is the masking binary matrix of same dimensions as the input image and composed by 1s (pixels to keep) and 0s (pixels to remove).

Remove lens distortion. Lens distortions are inherent to the mechanics and setup of a camera, and affect the way a camera maps the 3D world into a 2D image. The model used for such mapping can be estimated and compensated for errors up to a degree. This estimation is referred to as camera calibration and which, among other parameters such as radial and tangential distortions, provides the camera's intrinsic matrix K, as defined by Corke (2011). Aforementioned estimation was done by means of the Matlab® Calibrator App as described in Matlab (2018).

Orthorectify image. Given the platform used for capturing the data (i.e. a ship), images will present a perspective distorted view of the sea-ice field due to the angle difference between their optical principal axis and the normal axis of the horizontal plane (i.e. sea water in the present case). Geometric perspective transformations can, with limitations, recover the true shape of the captured environment. The approach presented here for geometrically orthorectifying an image is based on the camera coordinate system, transformation frames and matrices from robotics and the concept of homography which, in the context of computer vision, states that two distinct projections by a camera model of the same planar surface can directly be related through a homography matrix (see Corke (2011) and Sonka et al. (2014) for additional information). This relation is expressed as:

$$I' \simeq HI, \tag{2}$$

where I and I' are the original and rectified images respectively and H is the homography matrix, which

provides the required projective transformation up to a scaling factor, since homogeneous coordinates are used. In the ideal case of fully planar surfaces, the aforementioned relation is strictly accurate. For simplicity and given the scale of the measurements, it is assumed that the sea-ice forms an approximate planar surface.

Then, the homography matrix H is described in (3), where matrix K is the camera's intrinsic matrix and ${}^{W}_{C}R$ is a rotation matrix describing the camera's attitude in world frame, formulated in (4) and composed of an IMU's own attitude estimate ${}^{W}_{I}R$ and rotational relation to the camera ${}^{I}_{C}R$.

$$H = K\ {}^{W}_{C}R\, K^{-1} \tag{3}$$

$${}^{W}_{C}R = {}^{W}_{I}R\ {}^{I}_{C}R \tag{4}$$

Lastly, a detailed geometric derivation of a scaling factor *s=[mm/pixel]*, which relates pixel measurements in the orthorectified image with world measurements, is described in Sandru (2018).

2.2 Image processing

After the pre-processing phase, useful information can be extracted from the images, for instance discerning between ice/snow, slush and open water (i.e. image segmentation). Thresholding is one of the most common techniques used in image segmentation: based on their intensity value, pixels are classified in classes and/or grouped together according to one or more thresholds. The process of selecting the thresholding values can be manual (i.e. define static values), or automated through a clustering algorithm, such as the K-means algorithm (see Lloyd (1982), and Arthur and Vassilvitskii (2007) for an in detail explanation of the original algorithm and its improved version, respectively).

Several studies of surface albedo of ice, snow and open water, e.g. Brandt et al. (2005) or Zatko and Warren (2015), suggest a noticeable distinction between our proposed classes based on their light reflectance indices and, furthermore, imply one especially interesting idea: contrast among classes is increased based on the wavelength of the incident rays.

K-means. In short, the K-means algorithm (through an iterative process) tries to group a set of j observations (pixel values in an image histogram in our case) into k clusters or groups, by minimizing the overall distances within each cluster of the observations to the mean value (or centroid) of the cluster. In (5), $q_{x,y} \in [0, 1]$ corresponds to pixel intensity values at input image coordinates (x,y), $q'_{x,y}$ is the pixel value of the output segmented image at coordinates (x,y), classes k are defined as 1 for open water, 2 for slush, 3 for ice/snow and 0 for everything else, centroids are represented by C_i and sorted in ascending order based on their value. Note that $C_0 = 0$ and is ignored by the clustering algorithm. From (5) it can be noted that the thresholding values to segment pixels among classes are set as the mid-distance between two consecutive centroids.

$$q'_{x,y} = \begin{cases} 1, & 0 < q_{x,y} < (C_1 + C_2)/2 \\ 2, & (C_1 + C_2)/2 \leq q_{x,y} < (C_2 + C_3)/2 \\ 3, & (C_2 + C_3)/2 \leq q_{x,y} \leq 1 \\ 0, & q_{x,y} = 0 \end{cases} \tag{5}$$

Dynamic Thresholding. In such cases where imagery data acquisition is sequential and at sufficiently high rate (e.g. 1 Hz in our case), we propose that the K-means and thresholding algorithms can be fused together as follows: first, the K-means algorithm is run on the first image, thus obtaining a set of centroids which are used for segmenting the first and following image; second, a new centroid is obtained for each class by calculating the mean value in each class for the second image; third, the updated centroids from the second step are used for segmenting the following image; lastly, steps 2 and 3 are repeated for all the following images. This approach, referred to as DT (Dynamic Thresholding) thereon, aims at greatly reducing the computation cost inherent to the K-means algorithm.

2.3 Sea-ice floes detection and analysis

Once the image is properly segmented in classes and a scaling factor calculated, the analysis is focused towards extracting ice concentration and floes dimensions.

Morphological operations The first step is aimed at reducing the complexity of detecting individual ice floes by increasing their (pixel-wise) separation. One heuristic technique based on mathematical morphology involves morphological operations, particularly erosion and dilation (see Peterlin (1996) for additional explanations and details). Erosion shrinks an object area, while dilation increases it, by a factor determined by the structuring element's size and shape. Choosing the structuring element's size is a trade-off: on one hand a smaller size will separate only weakly connected ice floes, but their shape is highly preserved after the dilation process; on the other hand, a larger size will more effectively separate two connected ice floes, however their shape will be distorted after the dilation procedure.

Floe detection and analysis Objects detection (i.e. ice floes), their dimensions and ice/slush/open-water concentrations were obtained by means of image processing functions from Matlab (2019), particularly the following functions: *bwlabel* (identify individual 2D objects in an image) and *regionprops* (obtain details about a 2D object such as their major and minor axes, and area).

In the present work, first erosion is applied using a manually picked structuring element size and shape (static for a given input image resolution), then, object detection is performed and each detected ice floe is individually labelled. Next, a dilation operation is applied using the same structuring element to each individual ice floe and their individual dimensions obtained. Lastly, previous dimensions (in pixels) are transformed to world dimensions (in millimetres) using the scaling factor s from the orthorectification process.

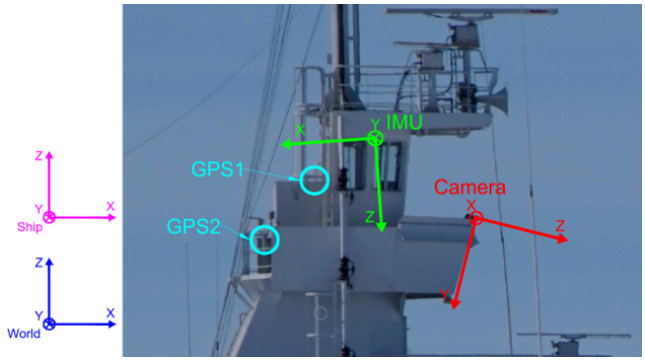

Fig. 3. Experimental setup installed in the crow's nest of S.A. Agulhas II. Superimposed, coordinate frames of the IMU, cameras, Ship and World.

3. EXPERIMENTS AND RESULTS

The experimental setup used for capturing data comprises a Basler machine vision camera (see Basler (2019)), two low-cost GPS antennas (for redundancy, see GlobalSat (2011) and u-blox (2008) for specifications), a commercial IMU (see MicroStrain (2007) for more details) and a standard PC equipped with four, 8 Tb hard disks (two of them allocated for backup). All sensors were set to record at 1Hz, except for the IMU, which was recording at 150Hz. Data collection was performed first, and the processing was done offline at a later stage. The data from the IMU was processed using the method detailed in Hyyti and Visala (2015), obtaining directly the rotation matrix ${}^{W}_{I}R$. Device synchronization was achieved through the PC's own clock, with an estimated accuracy in the order of few tens of milliseconds. This estimation is based on a comparison between each device's internal timestamp on the data (i.e. microcontrollers' ticks), and the PC's timestamp on the same data. The system was mounted in the crow's nest of the S.A. Agulhas II, as depicted in Fig. 3. Data capture was performed during the vessel's relief voyage to Antarctica in 2017-18.

In order to test the assumption that the highest contrast among classes (ice/snow, slush and open water) is achieved in the near UV spectra of light, imagery data was recorded in raw format and, using the camera's Bayes filter distribution, three distinct channels were obtained, namely red (R), green (G) and blue (B). A single row plot containing all three classes is depicted in Fig. 4.

At the current stage, it was not possible to obtain a ground truth which could be used to determine the accuracy of the orthorectification process in recovering the true shape (and dimensions) of the sea-ice floes. However, the error in the aforementioned accuracy can partly be estimated by using the ship's own width (from CAD drawings as true value) at a common location with the imagery data. This location was chosen to be the bottom row of the images, as shown in Fig. 5. The results of the expected estimation error are presented in Table 1, given as the measurement error percentage ± the discretization error (since the measurement is based on the distance between two pixels, discretization error is calculated as two times the scaling factor). Theta angle represents the angular difference between the camera's principal axis and normal

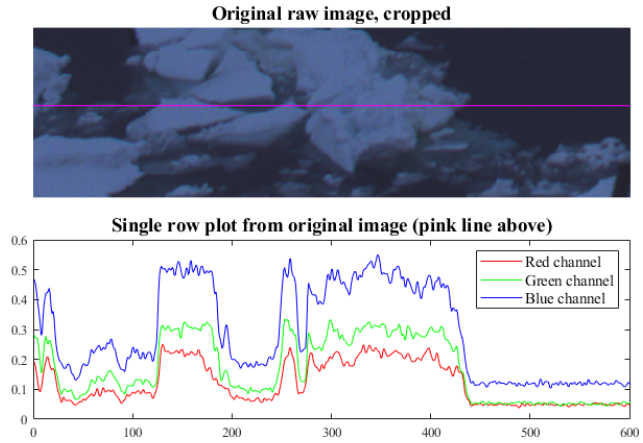

Fig. 4. Cropped raw image with highlighted row (top) and RGB channels plot of the same row (bottom).

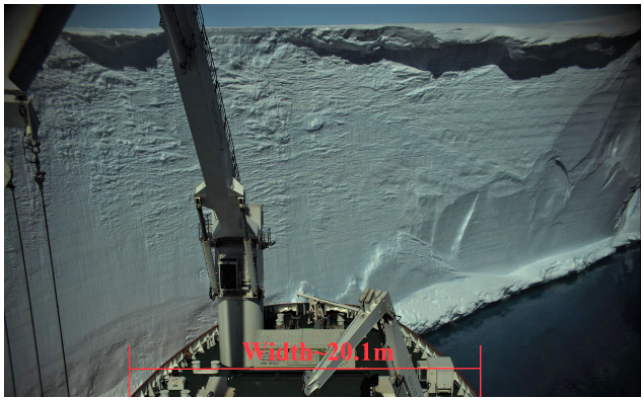

Fig. 5. Approximate width of S.A. Agulhas II at the last pixel row of an image.

axis of the horizontal plane. Height is measured between the camera centre and the deck rail. For the sea-ice analysis, a height of 34.1m was used instead for calculating the scale at water level.

Once the above has been established, in Fig. 6 the imagery output of a run sequence of the complete process is presented. The distance (in front of the ship) for orthorectification in Fig. 6g is manually selected, as well as the kernel sizes for the morphological operations before and after the K-means algorithm in Fig. 6h. Aforementioned kernel sizes are maintained static through the sequence run. Lastly, examples of potential statistics to be obtained are shown in Fig. 6j where *Major* and *Minor axis* are the mean measured major and minor axis of an ellipse which has the same normalized second moments as the detected ice floes, *Concentration Floes* refers to the concentration of the detected ice floes (see Fig. 6i), *Concentration Ice Total* refers to the total amount of ice detected by the

Table 1. Estim. of expected error at deck level

Theta angle (θ)	76°
Height	≈20m
Scale[m/px]	≈0.05
Measurement	20.79m (403pixels)
True value	20.1m
Expected error	3.43%
Discretization error	±0.10m

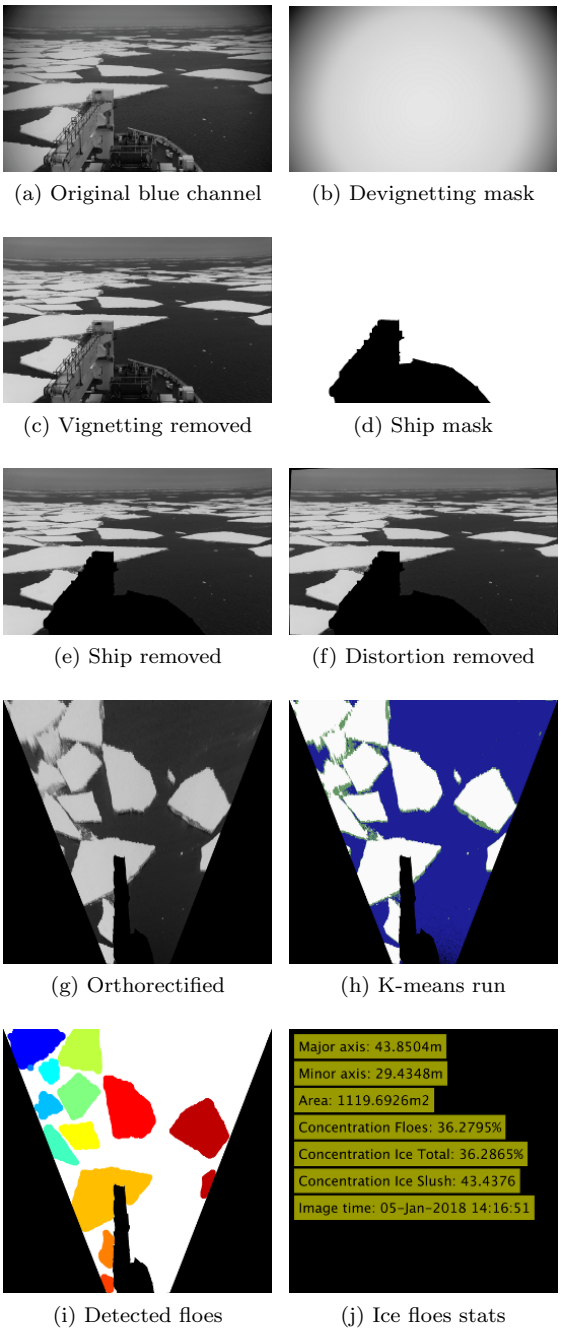

(a) Original blue channel (b) Devignetting mask

(c) Vignetting removed (d) Ship mask

(e) Ship removed (f) Distortion removed

(g) Orthorectified (h) K-means run

(i) Detected floes (j) Ice floes stats

Fig. 6. Visual presentation of a run sequence of the complete process

K-means algorithm (white areas in Fig. 6h), and lastly *Concentration Ice Slush* includes both the green and white areas in Fig. 6h.

Next, a comparison was performed between a set of selected images, where sea-ice floes boundaries were first manually identified and then using the K-means algorithm (see Fig. 7). The numerical mean statistics of the identified ice floes in both cases are depicted in Fig 8.

Single image analysis was performed using the K-means algorithm. However, for extended runs the proposed more efficient algorithm, DT, was utilized. As a consistency comparison, Fig. 9 represents a plot of the centroids for both algorithms for a sequence of 100 images. Only three

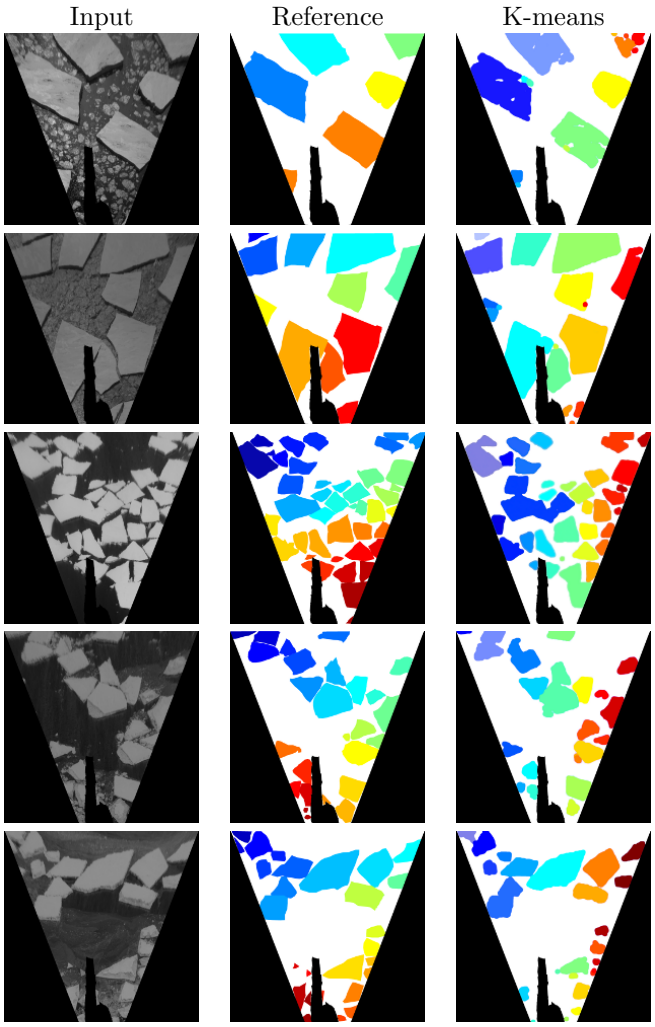

Fig. 7. Input images (left column); reference, i.e. manually identified ice floes (centre column) and using K-means (right column).

of the centroids are plotted, as the first is constant for both algorithms (i.e. $C_0 = 0$). It is worthwhile mentioning that the average processing time per image for K-means was around 10 seconds, while for DT it took 10 seconds for the first image, and ≈ 0.21 seconds for all the subsequent images. The processing was done using an Intel Xenon E3-1230 in Matlab environment.

Lastly, a sequence of images was analysed using DT, and compared with visual observations, where a (shortly trained) volunteer records ice thickness, concentration and floes sizes on a minute basis, which are then averaged over a period of 10 minutes and represent the colour intensity of each red block in Fig. 10. A more detailed description of the visual observations procedure can be found in Suominen et al. (2017).

4. DISCUSSION

The proposed devignetting method has successfully managed to obtain a mask and remove the vignette effect from images. The effects can also be noticed indirectly from the K-means algorithm: even though such algorithm was used on pixel intensities, it was not affected by the

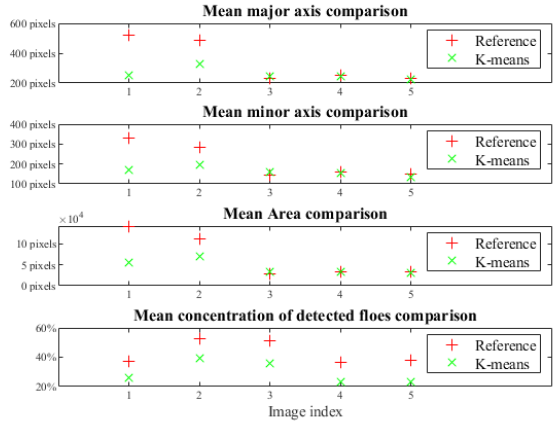

Fig. 8. Mean statistics comparison between manually delimited ice floes and using K-means algorithm.

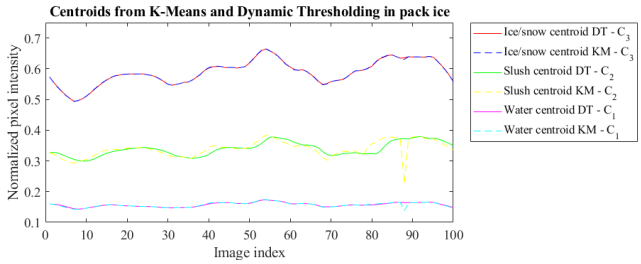

Fig. 9. Comparison of centroids values for K-means and Dynamic Thresholding, where the centroids for both algorithms behave similarly.

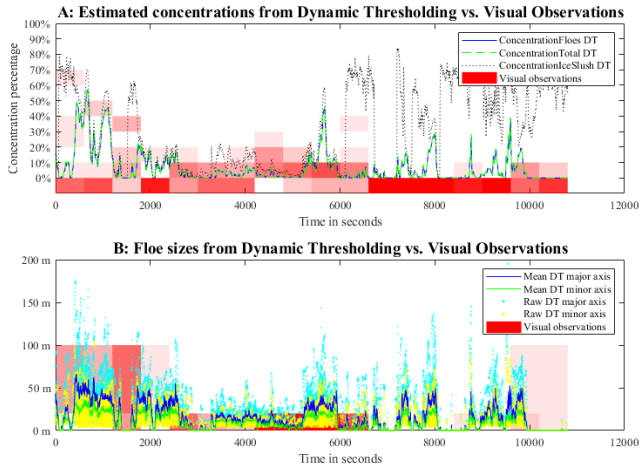

Fig. 10. Comparison between visual observations (background red rectangles) and Dynamic Thresholding analysis.

vignette effect, since the location of a floe in the image did not affect its detection. Nonetheless, additional verification tests need to be carried on, to certify the suitability of the method.

Even though a ground truth was not available, the use of the ship's width as a *measuring stick* proved beneficial in partially estimating the expected error in the calculated statistical data from the ice field. Such error could be minimized by using a higher resolution camera.

The proposed DT algorithm is comparable to the original K-means algorithm, as proved in Fig. 9 for a sequence of images with at least 1 Hz frequency, but offering much lower processing times. From Fig. 7 and 8 it becomes apparent that over-segmentation can present a challenge in accurately identifying ice floes and gathering correct statistics of the ice field. One simple solution would be to remove any detected ice floes under certain limit, for example 20 metres across. On the other hand, under-segmentation can in turn bias the acquired statistics towards higher values, and it presents its own challenges: a human observer may use other sources of information in order to discern whether two closely connected ice floes form two separate entities or one single ice floe. Sources of such extra information may be their relative movement against each other or even the shape and length of their connection point (i.e. an hourglass shaped ice floe with a narrow middle part would most certainly be composed by two distinct ice floes). All in all, further development is required and an additional layer of information added in order to effectively remove, or at least minimize, over and under-segmentation.

Regarding the proposed experimental setup, it is worth mentioning that a higher degree of sensor synchronization is desired, which would enable further analysis options. Nevertheless, this is acceptable given the slow dynamics of a ship. One addition would be the use of the Pulse Per Second (PPS) output from the GPS antenna in order to synchronize all capturing devices. On the other hand, the blue channel from the camera does indeed provide a higher degree of contrast among classes, which is highly beneficial in image segmentation.

Lastly, Fig. 10A and 10B present a clear benefit, matchless for humans: the proposed system can provide a much denser analysis, both temporal and by amount and type of retrieved information. The estimated concentrations from DT and visual observations in Fig. 10A are in good agreement for the first half of the sequence, however, DT highly overestimates the concentration of ice and slush (black line) for the second half. This is due to lack of ice and having set the system to forcibly detect four classes in any case. Therefore, the concentration estimate is assumed accurate as long as there is some amount of ice (green line in Fig. 10A). One additional benefit from the system is that a Region Of Interest (ROI) can be defined, thus obtaining an analysis not bound to the subjective perception of a person. It is worth mentioning that in Fig. 10B, at $t \approx 1200s$ DT is presented with open water imagery, while the human observer was most probably looking at a nearby large ice floe, hence the strong disagreement.

5. CONCLUSION

We proposed an automated process for sea-ice field analysis using machine vision cameras, inertial and satellite navigation sensors mounted on the crow's nest of a ship. With the proposed sensors and methods, we are able to estimate sea-ice concentration, floes size and distribution automatically in pack ice conditions. Data was collected on board the ice breaker S.A. Agulhas II during its relief voyage to Antarctica in 2017-2018. Our automated process

was compared to on-board manual visual observations, the current state-of-the art method for ice field analysis on board vessels. The results indicate that our method can give significantly more detailed and frequent information about individual ice floes, their sizes and shapes than any human observer is able to.

In the future, more development should be done to increase the accuracy and precision of the automated sea-ice floe detection method. Even better selection than the blue channel could possibly be found in the future work by using some combination of the color channels. Additionally, new controlled experiments should be made to verify the accuracy of our system and calibrate any estimation offsets or biases in the sea-ice floe concentration or mean size. As found in our work, the manual visual observations are not reliable enough to be used as a ground truth.

The initial results show that our automated sea-ice floe detection and analysis process has a great potential in providing valuable information for navigating a ship in ice infested waters and at the same time, collecting relevant environmental information about the sea-ice state.

ACKNOWLEDGEMENTS

Special thanks go to Dr. Annie Bekker from Stellenbosch University, who made possible a once in a lifetime trip for data collection. In addition, we would like to thank Jakke Kulovesi for providing the image capturing software, as well as Mikko Suominen for aiding with the preparations and ship instrumentation.

REFERENCES

Arthur, D. and Vassilvitskii, S. (2007). k-means++: The advantages of careful seeding. In *Proceedings of the eighteenth annual ACM-SIAM symposium on Discrete algorithms*, 1027–1035. Society for Industrial and Applied Mathematics.

Basler (2019). ava2300-25gc - basler aviator. URL `https://www.baslerweb.com/en/products/cameras/area-scan-cameras/aviator/ava2300-25gc/`. [Accessed: 2019-08-30].

Brandt, R.E., Warren, S.G., Worby, A.P., and Grenfell, T.C. (2005). Surface albedo of the antarctic sea ice zone. *Journal of Climate*, 18(17), 3606–3622.

Corke, P. (2011). *Robotics, Vision and Control: Fundamental Algorithms In MATLAB®*, volume 73. Springer.

GlobalSat (2011). GPS receiver BU-353S4. URL `https://www.globalsat.com.tw/en/product-199952/Cable-GPS-with-USB-interface-SiRF-Star-IV-BU-353S4.html`. [Accessed: 2019-08-30].

Hyyti, H. and Visala, A. (2015). A DCM based attitude estimation algorithm for low-cost MEMS IMUs. *International Journal of Navigation and Observation*, 2015.

Kang, S.B. and Weiss, R. (2000). Can we calibrate a camera using an image of a flat, textureless lambertian surface? In *European conference on computer vision*, 640–653. Springer.

Lloyd, S. (1982). Least squares quantization in PCM. *IEEE transactions on information theory*, 28(2), 129–137.

Lyu, S. (2010). Estimating vignetting function from a single image for image authentication. In *Proceedings of the 12th ACM workshop on Multimedia and security*, 3–12. ACM.

Matlab (2018). *Single camera calibrator app.* Matlab. URL `https://se.mathworks.com/help/vision/ug/single-camera-calibrator-app.html`. [Accessed: 2019-08-30].

Matlab (2019). *Image Processing Toolbox.* Matlab. URL `https://se.mathworks.com/products/image.html`. [Accessed: 2019-08-30].

MicroStrain (2007). *3DM-GX2® Datasheet.* MicroStrain®. URL `http://www.microstrain.com/inertial/3dm-gx2`. [Accessed: 2019-08-30].

Paget, M., Worby, A., and Michael, K. (2001). Determining the floe-size distribution of east antarctic sea ice from digital aerial photographs. *Annals of Glaciology*, 33, 94–100.

Peterlin, P. (1996). Morphological operations: an overview. URL `http://www.inf.u-szeged.hu/ssip/1996/morpho/morphology.html`. [Accessed: 2019-08-30].

Sandru, A. (2018). *Sea Ice Field Analysis Using Machine Vision.* Master's thesis, Aalto University. URL `http://urn.fi/URN:NBN:fi:aalto-201810175472`.

Sonka, M., Hlavac, V., and Boyle, R. (2014). *Image processing, analysis, and machine vision.* Cengage Learning.

Suominen, M., Bekker, A., Kujala, P., Soal, K., Lensu, M., et al. (2017). Visual antarctic sea ice condition observations during austral summers 2012-2016. In *International Conference on Port and Ocean Engineering under Arctic Conditions.* International Conference on Port and Ocean Engineering Under Arctic Conditions.

Tillman, H., Jian, Y., and Thor Nielsson, E. (2018). The polar silk road: China's new frontier of international cooperation. *China Quarterly of International Strategic Studies*, 4. doi:10.1142/S2377740018500215.

u-blox (2008). LEA-5H, LEA-5S, LEA-5A u-blox5 GPS and GALILEO modules. URL `http://www.mipsasoft.com/MS7/Hardware/Expansiones/Int8/GPS/GPS20UBLOX20LEA-5A.pdf`. [Accessed: 2019-08-30].

Weissling, B., Ackley, S., Wagner, P., and Xie, H. (2009). Eiscam - digital image acquisition and processing for sea ice parameters from ships. *Cold Regions Science and Technology*, 57(1), 49–60.

Zatko, M.C. and Warren, S.G. (2015). East antarctic sea ice in spring: spectral albedo of snow, nilas, frost flowers and slush, and light-absorbing impurities in snow. *Annals of Glaciology*, 56(69), 53–64.

Zhang, Q. and Skjetne, R. (2015). Image processing for identification of sea-ice floes and the floe size distributions. *IEEE Transactions on geoscience and remote sensing*, 53(5), 2913–2924.

Zheng, Y., Yu, J., Kang, S.B., Lin, S., and Kambhamettu, C. (2008). Single-image vignetting correction using radial gradient symmetry. In *IEEE Conference on Computer Vision and Pattern Recognition (CVPR), 2008*, 1–8. IEEE.